Journal of Hydrology xxx (xxxx) xxxx

Contents lists available at ScienceDirect

Journal of Hydrology

journal homepage: www.elsevier.com/locate/jhydrol

Research papers

Dynamics of seasonal snowpack over the High Atlas

Alexandre Tuel[a,*], Abdelghani Chehbouni[b,c], Elfatih A.B. Eltahir[a]

[a] Ralph M. Parsons Laboratory, Massachusetts Institute of Technology, Cambridge, MA 02139, USA
[b] InternationalWater Research Institute – Université Mohamed VI Polytechnique, Benguérir, Morocco
[c] CESBIO (CNES-CNRS-IRD_INRAE-UPS), Toulouse, France

ARTICLE INFO

This manuscript was handled by Marco borga, Editor-in-Chief

Keywords:
Empirical snow model
SNOW17
SWE
Morocco
Sublimation

ABSTRACT

Snowpack melting in the High Atlas constitutes the major source of freshwater for the semi-arid agricultural plains of central Morocco. Snow runoff fills dams during spring and recharges groundwater, thus providing the necessary water for irrigation and hydropower production. Despite its critical importance for the region, basic questions about the High Atlas snowpack remain largely unanswered. In particular, the spatial and temporal distribution of snow water equivalent, as well as sublimation losses, potentially significant in this region, have yet to be thoroughly investigated. The scarcity of ground data has been a major obstacle to investigating snow processes in the High Atlas. Here, we demonstrate the potential of remotely-sensed meteorological variables and downscaled climate reanalysis data to gain important insights into snow water balance in a semi-arid region. We apply a distributed energy balance snow model based on SNOW17, constrained by topographic data, meteorological data from satellites and high-resolution dynamically-downscaled ERA-Interim data, to simulate snowpack dynamics within the Oum-Er-Rbia watershed, at the heart of Morocco's High Atlas. The simulations are compared to MODIS snow cover maps and observed snow depth at one field station. Results show that the spatial extent and temporal dynamics of snow cover at various elevation ranges are accurately captured. The snowpack is essentially concentrated above 2500 m, extends over 500–6000 km^2 and holds 0.05–0.4 km^3 at its peak in early February. Additionally, we find that losses by sublimation range from 0.06 to 0.14 km^3 for an average of 0.09 km^3 a year, about 10% of all snowfall. Above 3000 m elevation, sublimation removes on average 20% of the snowpack. Finally, we discuss the sensitivity of our results to uncertainties in the forcing meteorological data. This study reveals the essential components of the snow water balance in the High Atlas and paves the way for better understanding of its sensitivity to climate change.

1. Introduction

While average annual precipitation hardly reaches at best 500 mm over Morocco's agricultural plains, the Atlas Mountains, which rise up to 4000 m high, usually receive up to twice that amount, most often in the form of snow between November and March (Boudhar et al., 2009). Consequently, mountain precipitation is a major source of freshwater for the country, especially its agriculture, which accounts for 90% of all water use. The melting of the winter snowpack during spring substantially contributes to river discharge – up to 50% in some local catchments (Boudhar et al., 2009), filling dams beyond the wet season and allowing for continued water use and irrigation until the end of the growing season in May. Infiltration of mountain runoff also accounts for much of the aquifer recharge, on which agricultural activities in the fertile plains at the foot of the Atlas critically depend (Chehbouni et al., 2008). Yet, although the importance of the mountain snowpack for water resources is well-established, much remains unknown about its characteristics and spatio-temporal dynamics.

Accurate estimates of Snow Water Equivalent (SWE) fields in the High Atlas are necessary to improve our understanding of the regional hydrology and thus water resources management. In addition, assessing the sensitivity of the snowpack to meteorological and climate variables is critical in order to project its response to climate change, which is expected to bring warmer and much drier conditions over Morocco in the near future (Tuel and Eltahir, 2020; Tuel et al., 2020). Still, the scarcity of ground measurements, combined to the complex regional topography and the large spatio-temporal variability in hydroclimate (Fayad et al., 2017; Tuel and Eltahir, 2018), create significant challenges to snowpack monitoring and estimation at the basin scale. Satellite-based snow cover maps can provide a good first estimate of the extent and temporal evolution of the snowpack, as was shown for the Atlas Mountains (Marchane et al., 2015). Where enough station data is

* Corresponding author.
E-mail address: atuel@mit.edu (A. Tuel).

https://doi.org/10.1016/j.jhydrol.2020.125657
Received 15 April 2020; Received in revised form 17 June 2020; Accepted 13 October 2020
Available online 17 October 2020
0022-1694/ © 2020 Elsevier B.V. All rights reserved.

Please cite this article as: Alexandre Tuel, Abdelghani Chehbouni and Elfatih A.B. Eltahir, Journal of Hydrology, https://doi.org/10.1016/j.jhydrol.2020.125657

available, complex physically-based snow models that resolve the energy balance at the surface, and may even include several snow layers (Liston and Elder, 2006; Herrero and Polo, 2016; Boudhar et al., 2016), are usually preferred. Recently, Baba et al. (2019) applied SnowModel, a physical snowpack evolution model based on the snow energy balance, to simulate snowpack dynamics in the Rheyara catchment of the High Atlas, outside our study zone, down to a resolution of 8 m. Their approach was made possible by the small size (220 km^2) of the catchment and its relatively high density of weather stations. The large data requirements of such models, however, make them less applicable over large areas, where even basic data like temperature is often missing. Therefore, essential questions remain unanswered for the High Atlas: most importantly, how much water is stored in the snowpack? And how does this amount vary in space and time?

At the catchment scale, conceptual, distributed snow models, typically based on simple parametrizations of melt as a function of temperature, and forced with remotely-sensed data, spatially interpolated station data or analytical mesoscale model output, can yield useful results (Marks et al., 1999; Clark et al., 2011; Raleigh and Lundquist, 2012). When ground data is particularly scarce or unavailable, one possibility is to resort to remotely-sensed snow cover maps and reconstruct SWE backwards in time using the observed snow fraction time series at each grid point as constraints (Molotch, 2009; Raleigh and Lundquist, 2012). An advantage of this approach is that it only requires temperature as input if no new snowfall accumulates after peak SWE; on the downside, it can only reconstruct SWE during the melt phase, is not useful to make SWE projections and is also very sensitive to biases in snow cover data (Molotch and Margulis, 2008). Often, forward configurations in which precipitation is partitioned between rain and snow and accumulated snowfall stored as SWE are preferred (Raleigh and Lundquist, 2012). In their simplest form, empirical snow models only require temperature and precipitation and temperature, although more complex formulations involving radiative fluxes are also available (Hock, 1999; Follum et al., 2015). Several previous studies that relied on station measurements have shown that they were able to satisfactorily estimate snow accumulation and melting in various climate zones, including the High Atlas (Follum et al., 2015; Boudhar et al., 2016; Bouamri et al., 2018). Such models have also been successfully applied to reconstruct SWE fields in various Mediterranean-climate regions (Shamir and Georgakakos, 2007; Guan et al., 2013; Fassnacht et al., 2017; Fayad et al., 2017). However, station data is often missing, which has led to increased interest in the applicability of gridded climatological datasets, like climatological reanalyses (e.g., ERA-Interim (Dee et al., 2011)), station-based interpolated datasets or satellite-based products, to be used as input to snow models (Muñoz et al., 2014; Shamir and Georgakakos, 2014). However, questions still remain as to their accuracy to represent fine-scale conditions in complex topography, especially precipitation maxima near mountain peaks (Muñoz et al., 2014). To circumvent that problem, reanalysis data can be downscaled to finer resolution with regional climate models (Wrzesien et al., 2017), an approach that has proved successful over several mountainous regions (Alonso-González et al., 2018 and reference therein). The forcing datasets can suffer from numerous biases, however, especially precipitation, which in complex terrain typically exhibits strong spatio-temporal variability that is hard to capture. Regional models can be unreliable since precipitation relies on parametrizations that require observations as input, and gridded satellite-based precipitation products, like TRMM (Huffman et al., 2007), CHIRPS (Funk et al., 2015) or GPM (Huffman et al., 2014), are often the only estimates available. Such products usually tend to underestimate snowfall and wet season precipitation in mountain regions (Derin et al., 2016; Hashemi et al., 2017), which may bias the results, particularly since parameter fitting of empirical snow models is typically highly sensitive to input uncertainty (Franz et al., 2010; He et al., 2011). Few studies seem to rely on satellite-based precipitation, preferring model-simulated precipitation (Wrzesien et al., 2017; Alonso-González et al., 2018) or global station-based products (Muñoz et al., 2014), when direct interpolation from local stations is not possible. In addition, one downside of previous such studies is the absence of explicit sublimation fluxes. Yet, because the High Atlas has a particularly arid climate, latent heat fluxes are significant: locally, 25–45% of accumulated snow has been found to be lost to sublimation (Schulz and de Jong, 2004; López-Moreno et al., 2017). Sublimation is known to vary significantly in space, especially in complex mountain regions (Strasser et al., 2008). Any snow model applied at the basin scale in this area should therefore include latent heat fluxes, which requires additional meteorological information, notably atmospheric humidity.

The innovative aspect of this study is in how we estimate the spatial and temporal distributions of snowpack water content and sublimation in a large area of about 13,000 square kilometers in the High Atlas, using a distributed physically-based snow model constrained by a combination of topographical data, remotely-sensed data, and meteorological data dynamically-downscaled down to 12 km. To our knowledge, no other study has attempted to assimilate data from such various sources to model snow in a data-scarce region. In addition, we model sublimation explicitly to provide the first estimate of the spatial distribution of latent heat fluxes in the High Atlas. Our focus is the Oum-Er-Rbia watershed, one of Morocco's major agricultural regions and an important producer of hydropower, which receives the most snowfall among all the country's main watersheds (Marchane et al., 2015) and depends almost exclusively on mountain precipitation. Satellite-based snow cover is used as a constraint in order to estimate snow model parameters. While previous studies have suggested that the strong spatial variability of Atlas snow cover warranted less than 500 m resolution (Baba et al., 2019), we select a resolution of 1 km for our model, based on data availability and computing power. Despite this limitation, snow modeling at such a resolution and spatial scale has never been attempted for the Moroccan Atlas. Our aim is to capture the main features of variability in snow cover and provide a first order characterization of the snow water balance of the basin.

2. Data and methods

2.1. Study area

The Oum-Er-Rbia, with its 550 km length and 3 km^3 annual discharge, is one of Morocco's major rivers. Its water supports 30% of the country's irrigated land, 50% of its hydropower capacity, and provides for the daily needs of seven million people, including two major cities, Casablanca and Marrakech. It flows northwestward from the northern slopes of the High Atlas, Morocco's largest mountain range. Our 13,104 km^2 study area covers the drainage basins of four main dams, corresponding to the major tributaries of the Oum-Er-Rbia, all located at the foothills of the High Atlas (Fig. 1). Elevation in the area ranges from 621 m to 3890 m, for a mean of 1882 m. Vegetation is sparse, consisting mostly in bare soil and grass and rare shrubs in areas where snow is present (Baba et al., 2019), with forest cover essentially limited to the valleys. The area is under a rather continental climate, characterized by a large amplitude of temperature annual cycles (Knippertz et al., 2003). Temperatures are minimal in January, when they range from mild (~12 °C) below 1000 m to cold (-5°C) above 3000 m. Even at that time, the foothills seldom go below freezing. By contrast, peak summer temperatures, occurring in July, are very high (35 °C) at the lowest elevations, and still quite warm above 3000 m (10–15 °C) (Ouatiki et al., 2017). Conditions are overall quite dry, even at high elevations, where annual precipitation reaches 800–1000 mm, against lows of 250 mm in the plains to the west. About 80% of annual precipitation occurs during the wet season, from October to April, when the region is under the influence of North Atlantic westerlies which bring the occasional storm systems responsible for most of the precipitation (Knippertz et al., 2003; Tuel and Eltahir, 2018). Above 1500 m, snowfall is common during the winter months. Persistent snow

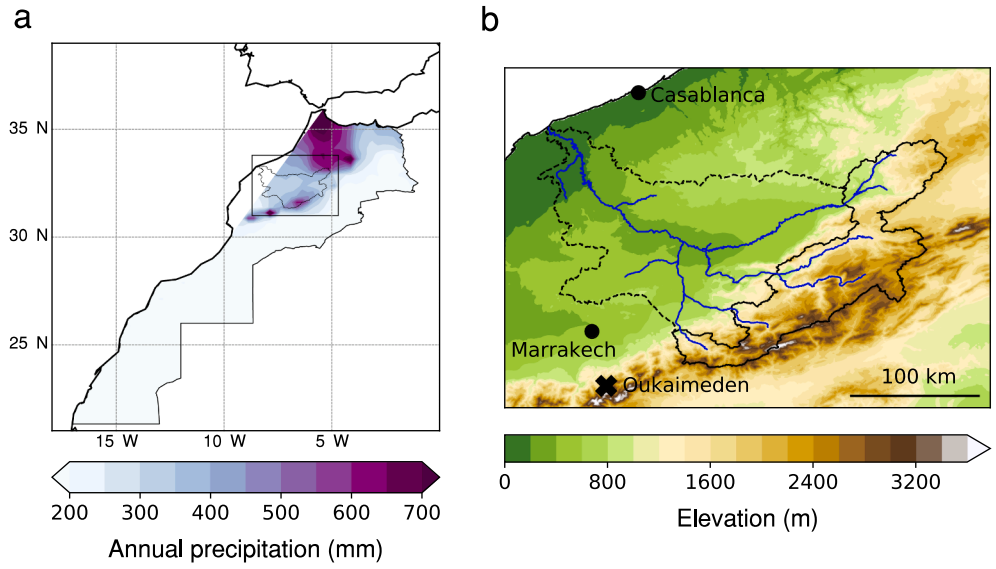

Fig. 1. (a) Annual precipitation over Morocco (TRMM data, see text) and Oum-Er-Rbia watershed. (b) Study area (solid black line) within the Oum-Er-Rbia watershed (dashed line), with elevation in shaded contours, main cities (dots), river network and snow station (cross).

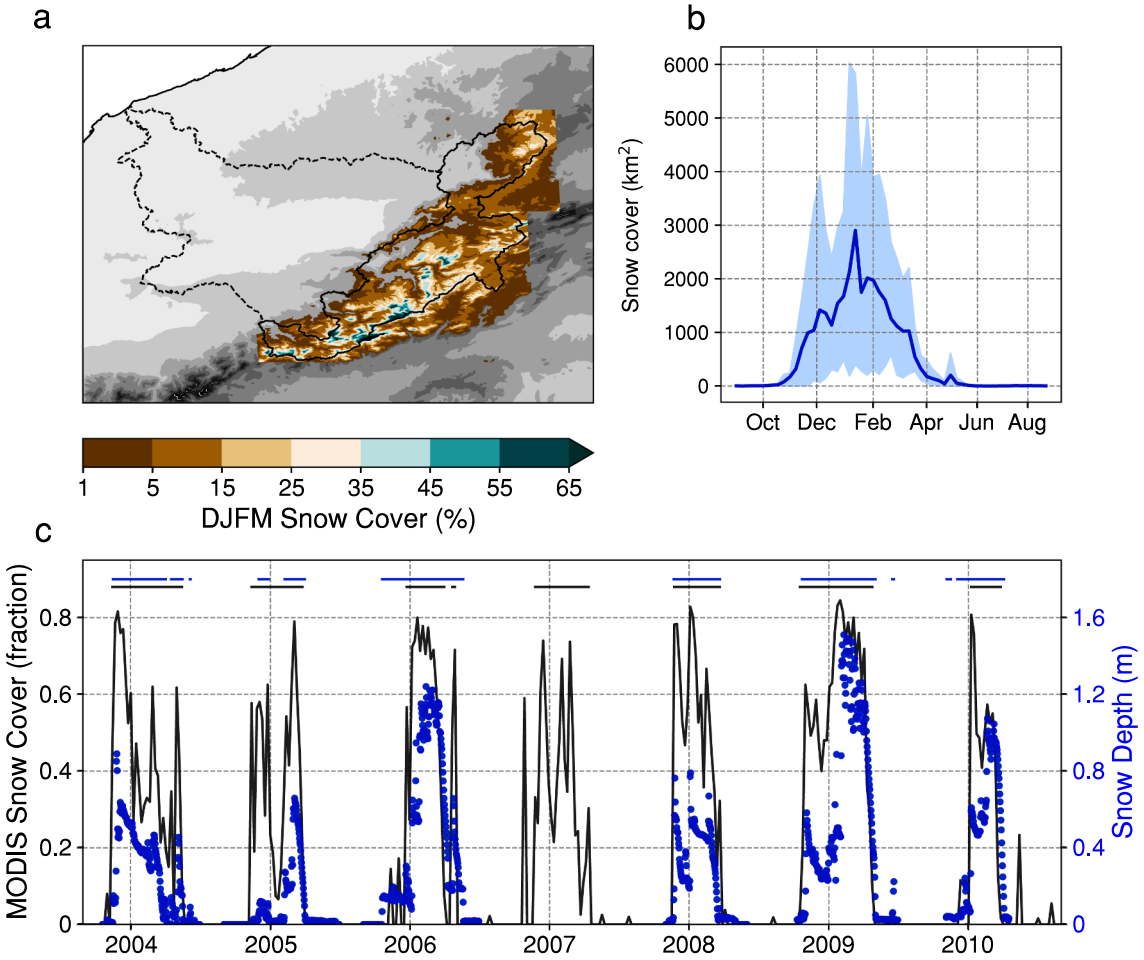

Fig. 2. (a) December-March average snow cover in the Oum-Er-Rbia basin, from MOD10A1 v6. Data outside the direct neighborhood of the study area is not shown. (b) Annual cycle of snow cover extent in our study area (mean: solid blue line, 90% range: blue shading). (c) Time series of weekly mean snow depth measured at Oukaimeden station (blue dots) and fractional snow cover for the corresponding 500 × 500m MOD10A1 grid cell (black line). Horizontal bars at the top highlight periods with more than 5% snow cover or 5 cm snow depth.

cover is frequent above 2500 m, typically extends from December to April, and rapidly disappears by the end of May (Boudhar et al., 2010) (Fig. 2), though inter-annual variability is substantial (Marchane et al., 2015). Our study area encompasses most of the zones in the Oum-Er-Rbia watershed that receive at least modest snow amounts on average during the winter (Fig. 2).

High Atlas snow cover is characterized by substantial variability in both space and time, a key feature in arid environments (Boudhar et al., 2010). At the annual time scale, wet season precipitation exhibits a large inter-annual variability (Knippertz et al., 2003), with a coefficient of variation of about 0.3 (Tuel and Eltahir, 2018), a variability that is reflected in seasonal snow extent (Marchane et al., 2016). Within a season, precipitation also tends to occur in short and irregular storm events; warm temperatures over a few dry weeks can lead to complete disappearance of the snowpack even in mid-winter at high elevations (Schulz and de Jong, 2004). Because net radiation dominates the snow energy balance (López-Moreno, 2017), snow cover is also highly dependent on terrain slope and aspect, with bare ground not uncommon even at high altitude (Marchane et al., 2015).

2.2. Snow model

In Mediterranean mountains, the snow energy balance is largely dominated by radiative fluxes (López-Moreno et al., 2017; Boudhar et al., 2016). Therefore, we select the radiation-derived temperature index (RTI) melt formulation (Follum et al., 2015, 2019), within the framework of the SNOW-17 model (Anderson, 2006). SNOW-17 simulates snow accumulation and loss empirically, using meteorological variables to account for the various energy balance equation terms. The main difference in this paper with the Follum et al. (2015) study is that we add a sublimation module, based on a bulk-aerodynamic flux formulation. We give here a brief summary of model structure (see Fig. 3) and equations; readers are referred to Follum et al. (2015) and Anderson (2006) for more details.

RTI uses a proxy temperature T_{rad} calculated from the surface radiation balance, instead of actual air temperature, to estimate snow melt. It therefore includes spatial variability in potential melt due to variability in incoming shortwave and longwave. T_{rad} is given by the following:

$$T_{rad,t} = \left(\frac{LW_{\downarrow} + (1-\alpha)SW_{\downarrow} - LE}{\epsilon_s\ \sigma}\right)^{1/4} \tag{1}$$

where $LW_{\downarrow}$ is the downward longwave radiation, $SW_{\downarrow}$ downward shortwave, α snow albedo, LE the latent heat flux (see below), ϵ_s the snow surface emissivity (taken to be 1) and σ the Stefan-Boltzmann constant. Although equation (1) neglects many terms of the energy balance (e.g., ground heat flux, sensible heat flux), at first order, T_{rad} represents the snow surface temperature that balances net surface radiation and can be interpreted as a measure of the amount of energy available to heat/melt the snowpack. In particular, T_{rad} can be above 0 °C. Short- and longwave are calculated as in Follum et al., 2015 (see section 2.3.6), with the exception that we assume no vegetation cover, an approximation we make due to the High Atlas' sparse vegetation. Tree cover is present at lower elevations (below 1500 m), where snow cover is short-lived due to relatively high temperatures. Snow albedo is parametrized according to the formula proposed by Brock et al. (2000) and calibrated for the High Atlas by Boudhar et al. (2016):

$$\alpha = 0.8 - 0.21\log_{10} t_d \tag{2}$$

where t_d is the number of days since last snowfall. Fresh snow albedo is set at 0.8, a low value but which best fits observations in the High Atlas, likely connected to the high concentration of mineral dust due to the proximity of the Sahara Desert (Xu, 2018).

Air temperature T_a is used to determine the phase of precipitation: we assume it will fall as snow if $T_a$is below 0 °C. Snowpack is characterized by its snow water equivalent SWE (in mm) and its heat deficit D_t, a measure of the energy needed to bring the snowpack to its melting temperature (0 °C). The heat deficit is expressed in mm of snow water equivalent (Anderson, 2006). At each time step, the heat deficit is updated as new snow falls, as snow sublimates or as energy is transferred from the atmosphere to the snowpack. The change in heat deficit due to differences between snowpack and air temperatures is expressed as:

$$\Delta D_t = NMF\cdot(ATI - T_{snow}) \tag{3}$$

where ATI is the antecedent temperature index (in °C), T_{snow} is the snow surface temperature, and

$$NMF = NMF_{max}\cdot\frac{SW_{12h,t}}{\max(SW_{12h,t})}\cdot dt \tag{4}$$

where NMF_{max} is the maximum negative melt factor (in mm/°C/hr), $SW_{12h,max}$ is the incoming shortwave radiation at noon on a flat surface on the current day and $\max(SW_{12h,t})$ its maximum value across the whole year. dt is the time step (in hr), here chosen to be 6. Snow surface temperature is parametrized as in Boudhar et al. (2016): $T_{snow} = \min(0,\ 0.72\cdot T_a - 2.47)$. In the case of a positive latent heat flux LE, the heat deficit is reduced proportionally to the amount of snow lost by sublimation during the time step:

$$\Delta D_t = -\frac{\frac{LE}{L_s}\cdot 3600\cdot dt}{SWE_t}\cdot D_{t-1} \tag{5}$$

where L_s is the latent heat of sublimation (2.834 MJ/kg).

Melt can occur once the heat deficit reaches 0. If less than 1.5 mm of rain occurred during the previous 6 h, melt is calculated by

$$M = \mathrm{dt}\cdot M_f\cdot T_{rad} + 0.0125\cdot p\cdot f_r\cdot T_r \tag{6}$$

with M_f the melt factor, p precipitation (mm), f_r equal to 1 if T_a is larger than 0 °C, 0 otherwise, and T_r is the precipitation temperature (maximum of 0 °C and T_a). Otherwise, melt is given by

$$M = dt\cdot\sigma((T_{rad}+273.15)^4 - 273.15^4) + 0.0125\cdot p\cdot f_r\cdot T_r + 8.5$$
$$\cdot f_u\cdot\frac{dt}{6}((\mathrm{rh}\cdot e_{sat} - 6.11) + 0.00057\cdot P_a\cdot T_a) \tag{7}$$

where $f_u = 0.5$ mm/mbar/6hr, rh is the relative humidity, e_{sat} the saturation vapor pressure (mb), and P_a the air pressure (in mb). e_{sat}, taken over water for $T_a \geq 0$ and ice otherwise, is calculated as in Alduchov and Eskridge (1996); P_a is assumed to be constant with elevation H, given by $P_a = 1013.25\cdot(1 - 2.25577\cdot 10^{-5}H)^{5.25588}$.

Eqs. (3)–(6) involve three parameters: M_f, NMF_{max} and $TIPM$ (used to calculate ATI, see Anderson, 2006) which must be calibrated. The

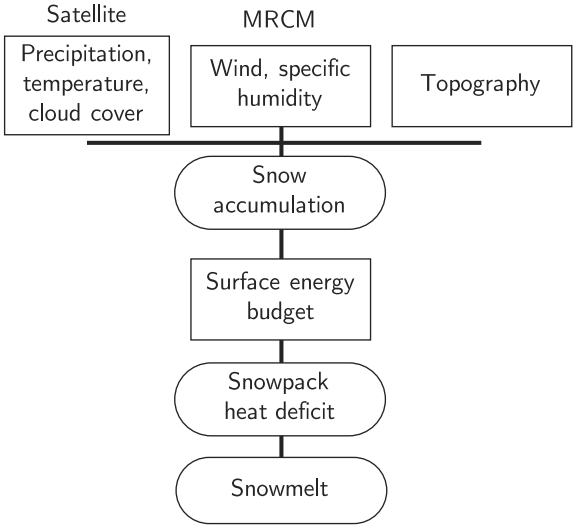

Fig. 3. Schematic of SNOW17.

RTI originally also includes another parameter, PLWHC, the relative fraction of liquid water holding capacity to the snowpack, which we take to be fixed at 0.05.

We parametrize sublimation based on the bulk-aerodynamic method, which assumes the latent heat flux (LE, in W/m^2) to be proportional to wind speed and water vapor gradient between the surface and a given level z:

$$LE = FSC \cdot \frac{f \cdot L_s \cdot \rho \cdot \kappa \cdot U(z) \cdot (q(z) - q_s)}{\log\left(\frac{z}{z_0}\right)^2} \quad (8)$$

where FSC is the grid cell fractional snow cover, ρ is air density (kg/m^3), κ is the von Karman constant, $U(z)$ and $q(z)$ are respectively the wind speed (m/s) and specific humidity (kg/kg) at height z, q_s is the surface specific humidity (kg/kg), z_0 is the surface roughness length (set to 0.001 following Boudhar et al., 2016), and f is a non-dimensional stability factor defined based on the bulk Richardson number $Ri = 9.81 \cdot \frac{(T_a - T_{snow}) \cdot (z - z_0)}{(T_a + 273.15) \cdot U(z)^2}$ (Anderson, 1976; Brutsaert, 1982):

$$f = \begin{cases} 1 if Ri = 0 \\ (1 - 5 \cdot Ri)^2 if Ri < 0 (unstable) \\ (1 - 16 \cdot Ri)^{0.75} if Ri > 0 (stable) \end{cases} \quad (9)$$

q_s is calculated assuming surface saturation at T_{snow}.

The model estimates SWE at each grid cell; we translate it to snow cover using the following formula:

$$SC = 0.85 \cdot \tanh(k \cdot SWE) \quad (10)$$

with $k = 100\text{m}^{-1}$ (Boudhar et al., 2011) and SWE in meters. We discuss (10) further in section 3.2. 0.85 is selected as maximum allowable snow cover due the quasi-absence of grid-scale (500 m) snow fractions larger than 85% in satellite observations. This likely reflects the strong small-scale variability of snow cover in the High Atlas at high altitudes (Baba et al., 2019).

Due to the large number of grid cells and associated computing time, the three parameters (M_f, NMF_{max} and $TIPM$) are fitted by maximizing the Nash-Sutcliffe coefficient (Nash and Sutcliffe, 1970) between the observed and simulated snow cover at 250 randomly selected grid points, at altitudes representative of the distribution of altitudes across the whole basin. To test the applicability of the RTI-SNOW17 model, and compare our results with those of Boudhar et al. (2016), we also fit the parameters to the observed snow depth series at Oukaimeden, using the TRMM precipitation estimate for the corresponding grid cell. SWE in the model is converted to snow depth (SD) (to compare with Oukaimeden measurements only) with the formulation used in Bouamri et al. (2018):

$$\text{SD}(t) = \text{SWE}(t) \times \frac{\rho_w}{\bar{\rho_s}(t)} \quad (11)$$

with $\rho_w = 1000\text{kg/m}^3$ (density of liquid water) and $\bar{\rho_s}$ is snowpack density, calculated as the average between the density of the previous snowpack:

$$\rho_s(t) = (\rho_s(t - dt) - \rho_{\max}) \times e^{\frac{\tau_f}{\tau} \cdot dt} + \rho_{\max} \quad (12)$$

and that of fresh snow $\rho_{\text{new}} = 67.9 + 51.3 \times e^{\frac{T_a}{2.6}}$ (Hedstrom and Pomeroy, 1998). $\tau_f/\tau = 0.24/4800\text{s}^{-1}$ is a characteristic time of density evolution.

2.3. Data

2.3.1. Station data

Quality checked data is available at the Oukaimeden automatic weather station, located at 3200 m altitude near the Oukaimeden ski resort, about 75 km away from the border of our study region (Fig. 1-b) in a similar physio-geographical setting. Daily snow depth is available for 6 seasons (2003–2006 and 2007–2010), and daily air temperature, relative humidity and 2-meter wind speed are available from 2003 to 2016, with occasional gaps (5–14% of the data depending on the variable). 30-minute air temperature was also measured from 2010 to 2018. Daily precipitation data is not available at the station, but only at the nearby CAF (Club Alpin Français) station located 600 m downslope, for the 1989–2010 period.

2.3.2. MODIS snow cover

For snow cover data, we use the MODIS Terra snow cover daily L3 product (MOD10A1) at 500 m resolution (Hall and Riggs, 2016). The data is available from late February 2000 to present. Snow cover is detected based on the Normalized-Difference Snow Index (NDSI), calculated from reflectances in the visible/near infrared and middle infrared. Snow cover fraction is then estimated from the NDSI using an empirical relationship fitted to high-resolution LANDSAT images from various regions of the world. Because of frequent cloud (~30%) cover in the High Atlas during the wet season, many data are missing or potentially misclassified. We apply the filtering algorithm introduced by Marchane et al. (2015) to filter missing data at the daily timescale, and then average snow cover at a weekly timescale. By comparing to station data and high-resolution (8 m) FORMOSAT-2 images, Marchane et al. (2015) found that, using this filtering process, the MOD10A1 product was able to accurately reproduce snow cover area in Morocco's mountains, including the timing of onset and melt. Fig. 2-c shows the correspondence between observed snow depth and MODIS fractional snow cover for the Oukaimeden station.

2.3.3. Topography

Elevation data is derived from the Shuttle Radar Topography Mission 90-meter resolution dataset version 4.1 (STRM90) (Jarvis et al., 2008), and resampled by bilinear interpolation to the MODIS land surface temperature resolution of about 1 km.

2.3.4. Surface temperature

Spatially distributed air temperature is derived from the global MODIS Land Surface Temperature (LST) product MOD11A1 L3 version 6 at 1 km resolution (Wan et al., 2015). MOD11A1, available from February 2000 to present, provides an estimate of land surface temperature based on clear-sky thermal infrared brightness temperatures, twice every 24 h (daytime measure at 10:30 and nighttime measure at 22:30 local solar time). The underlying algorithms rely on additional MODIS data for local corrections, including snow and cloud cover, emissivity, or water vapor. Details of the algorithm can be found in Wan (2008). The MODIS LST data was shown to be accurate within 1 °C in clear-sky conditions for snow-covered areas above −15 °C (Hall et al., 2008), below which air temperature seldom goes in the High Atlas. The strong correlation between LST and air temperature T_a has been documented in a number of studies, notably over snow cover (Hachem et al., 2012; Wang et al., 2013), with root-mean square errors of up to 4–5 °C in cold mountain environments (Williamson et al., 2014). MODIS LST has been used for distributed snow modeling with SNOW-17 by Shamir and Georgakakos (2014) in the mountains of Turkey, who found that LST-derived air temperature was highly correlated to station temperature (r = 0.93) and performed well in estimating snow mass and maximum SWE.

There are three main challenges associated with the use of LST for snow modeling. First, thermal satellite LST data collection is impossible under cloud cover, since cloud-top temperatures are measured instead (Ackerman et al., 1998). Many LST data are therefore missing and need to be filled. Second, although highly correlated, LST and air temperature are not the same, and a correction needs to be applied. Third, LST is measured only twice a day, and we need to infer its daily cycle in order to run a snow model at 6-hour time steps.

2.3.4.1. Filling of missing LST values. We fill missing LST values for daytime and nighttime series separately, by first calculating the daily

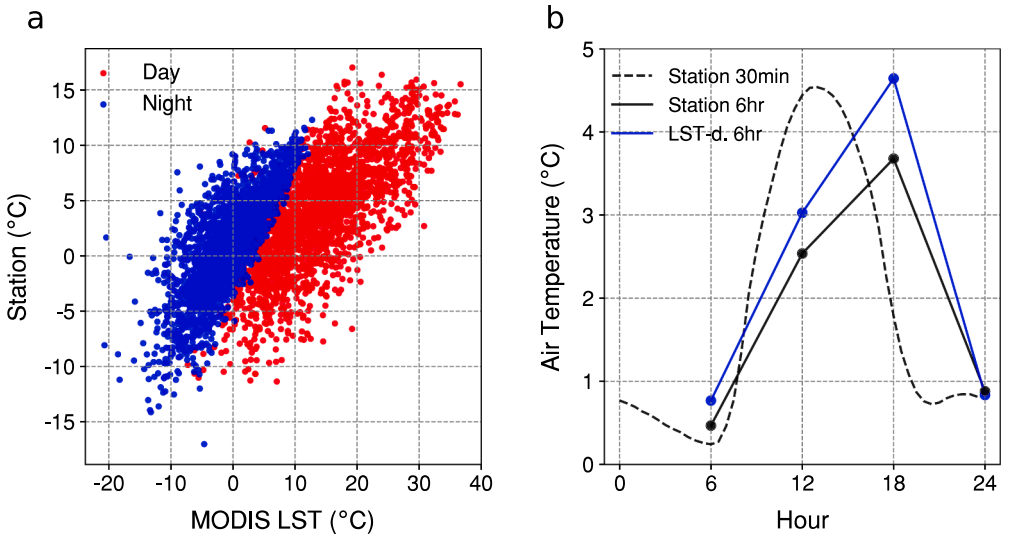

Fig. 4. (a) Air temperature measure at Oukaimeden station against the corresponding MODIS LST value, for daytime (red) and nighttime (blue) measurements. (b) Daily cycle of air temperature at the Oukaimeden station (dashed black line: 30-minute time step; solid black: 6-hourly) and 6-hourly cycle of MODIS LST-derived air temperature (blue).

deviation to an estimated annual LST cycle, and then interpolating missing values in both space and time. Since fewer than 20 years of data are available for any single day of the year (and even less for some grid cells due to cloud cover), and since LST can vary wildly on any given day, we estimate an annual cycle for LST at each grid point by averaging LST data for each week of the year. Then, we interpolate anomalies relative to that annual cycle as follows: for each 50 km-square in our domain, if less than 75% of data is missing, interpolation is performed spatially using 2D-kriging with an exponential semivariogram, fitted over the full area for all days and years available in the week of interest. If not, then interpolation is performed temporally using an autoregressive model of order 1 fitted to the time series of LST anomalies at each grid point.

2.3.4.2. Derivation of air temperature from MODIS LST. In general, the difference between LST and T_a is positive during the day, as solar radiation warms up the land surface, and negative at night, because the land surface cools faster than the air (Fig. 4-a). The LST-T_a relationship has been extensively studied, both theoretically and empirically. The general conclusion is that it depends on local variables, such as land cover, terrain aspect, the presence of snow, or soil moisture (e.g., Mildrexer et al., 2011). Here, we apply a simple linear correction $T_a = \alpha \cdot LST + \beta$ inferred from the 30-minute air temperature data measured at Oukaimeden station. We select the closest station measurement for each LST value in the Oukaimeden grid cell, and estimate regression coefficients α, β for each three-month period October-December, January-March, April-June and July-September, and for day- and nighttime measures separately. The resulting RMSE is found to be 3 °C. The same correction is assumed valid for the whole basin, admittedly a very broad assumption, justified here however by our lack of additional station temperature data.

2.3.4.3. Daily cycle. To interpolate the daily temperature cycle to 6-hour time steps (0, 6, 12 and 18 h local time), a common approach is to rely on harmonic functions (e.g., Shamir and Georgakakos, 2014). However, daily cycles of LST and air temperature do not appear to match sine waves (Fig. 4-b), so we opt for a different formula. At each grid point, the hour of sunset and sunrise are calculated based on day, slope and aspect (Duffie and Beckman, 2013). The nighttime LST-derived T_a is assumed representative for the whole night, from two hours after sunset till sunrise. Between sunrise and the daytime LST measure, LST-derived T_a is linearly interpolated. Between the daytime measure and two hours after sunset, it is interpolated using a second-degree polynomial with a maximum forced at two hours after solar noon. At the Oukaimeden station, the resulting LST-derived daily cycle of air temperature is on average within 0.5 °C of the observations (Fig. 4-b).

2.3.5. Precipitation

In complex, mountainous terrain with little to no station data, as is the case of the High Atlas, precipitation data from high-resolution satellite-based products is often the only option available. Here, we use 6-hourly precipitation from the TRMM TMPA (TRMM Multi-Satellite Precipitation Analysis) 3B42 version 7 dataset, which provides 3-hourly precipitation estimates by combining remotely-sensed data and correcting with rain gauge data on a monthly basis (Huffman et al., 2001). TRMM was selected for its relatively high spatial and temporal resolution and its overall better performance over our region compared to CHIRPS and GPM. TRMM data covers the period 1998 to present. It suffers from numerous biases, particularly at high elevations. First, accurately capturing snowfall remains challenging, particularly over snow surfaces. Second, in regions with few stations, gauge correction is uncertain, and made difficult by the topography (e.g., rain shadows). Third, TRMM tends to underestimate wet season precipitation, a particular concern in the present case (Milewski et al., 2015; Derin et al., 2016; Hashemi et al., 2017; Ouatiki et al., 2017). The accuracy of the TRMM 3B42 V7 dataset was evaluated over the Oum-Er-Rbia watershed by Ouatiki et al. (2017). While TRMM precipitation is unreliable at the daily timescale, its quality improves when averaged in space and time; at the annual time scale, they found RMSE values of 150–250 mm for stations at 1600–1800 m altitude. A large part of the bias occurs during summer, when local convective events are badly captured, but underestimation of winter precipitation is also important in mountain stations. Their results are consistent with those of Milewski et al. (2015) who analyzed TRMM V7 data over northern Morocco, including the Oum-Er-Rbia. At the location of the only currently available high-altitude station (CAF station), TRMM indicates an average of 725 mm of precipitation from November to April, against 350 mm measured at the station. Still, topography varies substantially within the 25x25km TRMM grid cell, ranging from 1000 m in the valleys to 4167 m at the Jbel Toubkal, Morocco's highest peak. Despite its deficiencies, TRMM remains our best baseline to estimate precipitation in this rugged and ungauged terrain.

2.3.6. Cloud cover

To calculate downward longwave and shortwave, we adopt the formulations of Follum et al. (2015) used in the GHSSA model (Downer et al., 2006):

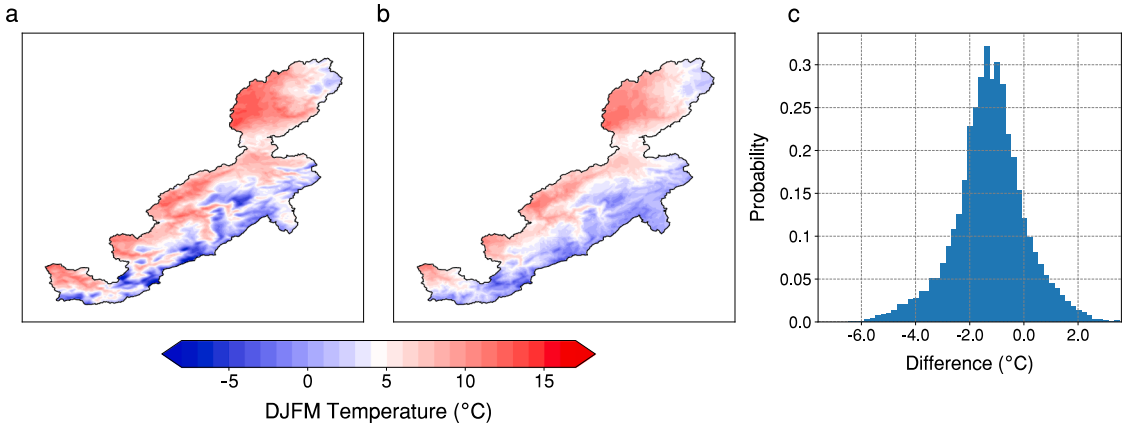

Fig. 5. December-March average temperature in our study area: (a) MODIS LST-derived, (b) MRCM interpolated to 1km resolution with elevation lapse-rates, and (c) histogram of the difference ((a) minus (b)).

$$\begin{cases} SW_{\downarrow} = S_0 K_r K_{atm} K_c K_s K_t \\ LW_{\downarrow} = \sigma \cdot \epsilon_a \cdot (T_a + 273.15)^4 \cdot (1 + 0.17N^2) \end{cases} \quad (13)$$

where $S_0 = 1366 W/m^2$ is the solar constant, ϵ_a is air emissivity (taken to be 0.757 when snow is present), N is fractional cloud cover and the K factors are coefficients of reduction of incoming solar radiation due to Earth-Sun distance (K_r), atmospheric scattering (K_{atm}), cloud absorption (K_c), terrain slope and aspect (K_s) and topographic shading (K_t). The daily cycle of solar radiation is included in K_s. In particular, $K_c = 1 - 0.65N^2$. We estimate N from the Terra MODIS MOD06_L2 version 6 cloud cover dataset (Platnick et al., 2015), available at 5 km-resolution from late February 2000 to present. The data is first linearly interpolated to extract 6-hourly time series. Over the whole available period, 9 sequences of more than two consecutive days are missing, during which MODIS LST data is also unavailable. In these cases, we randomly sample cloud cover values at each grid cell among non-missing values in the same cell and during the same month. Finally, the data is resampled at the MOD10A1 1 km resolution selected to run the model.

2.3.7. High-resolution dynamical downscaling of ERA-Interim

For humidity and wind data, we rely on dynamically-downscaled output from the MIT Regional Climate Model (MRCM) forced with ERA-Interim (Tuel et al., 2020). MRCM is based on the Abdus Salam International Centre for Theoretical Physics Regional Climate Model Version 3 (RegCM3), but with significant enhancements of model physics, and notably a coupling with the Integrated BIosphere Simulator land surface scheme (IBIS). Dynamical downscaling is performed for the 1982–2011 period at a resolution of 12 km. Details of the simulation, including model setup and performance, can be found in Tuel et al. (2020).

We extract 6-hourly 2-meter wind speed u, specific humidity q and air temperature T_a over our domain. Air temperature is used only to compare to the MODIS LST-derived estimates. Since the 12 km resolution is too coarse to account for all the sharp elevation gradients, we downscale specific humidity and temperature using 1 km elevation and altitude lapse rates estimated at each time step. Wind speed is left unchanged. Within a 12-km MRCM cell with temperature T_{12}, humidity q_{12} and elevation z_{12}, the downscaling to the 1 km grid cell with elevation z is given by:

$$\begin{cases} T_a = T_{12} + \lambda \cdot (z - z_{12}) \\ \log(q) = \log(q_{12}) + \mu \cdot (z - z_{12}) \end{cases} \quad (14)$$

where λ, μ are elevation lapse-rates, estimated from the MRCM output at each time step.

2.4. Model configuration and experiments

We run the snow model at a 6-hourly time step over the 2001–2011 period (10 hydrological years), during which all the forcing data is available, at the native MODIS LST (MOD11A1) resolution, of about 1000 by 1000 m. While that resolution may not be ideal to account for the small-scale variability in snow cover characteristic of the High Atlas (Baba et al., 2019), we select it here as a compromise between resolution and computation time. For comparison, 1 km^2 is the resolution at which SNOW17 is run over the coterminous United States within the Snow Data Assimilation program (Carroll et al., 2006). To check our results, we also ran the model at a 500 m resolution over the whole basin, and found no significant difference with the 1 km experiment. To test the sensitivity of the results to uncertainties in the forcing data, specifically temperature and precipitation, we fit the snow model under several configurations. First, three experiments in which an offset of respectively −3, 0 and 3 °C is applied to the LST-derived air temperature, with precipitation kept constant. We refer hereafter to these experiments as “LST-3”, “LST + 0” and “LST + 3”. The “LST + 0” experiment is also considered to be the control experiment. Second, in the fourth experiment (“TRMM + 33%”) TRMM precipitation is amplified by 33%, under unchanged LST-derived air temperature. Finally, we also assess the influence of the choice of SWE-snow cover relationship by fitting the snow model to a more conservative version of (10): $SC = 0.8 \cdot \tanh(k \cdot SWE)$ with $k = 40$ (the two relationships can be compared on Fig. 7-b.). We refer to this experiment as “SC40”. Optimized model parameters are determined for each experiment as described in section 2.2.

3. Results and discussion

3.1. Comparison of MRCM output with MODIS temperature data and Oukaimeden station data

Fig. 5 shows the December-March mean daily LST-derived air temperature and the corresponding MRCM field. Overall, there is relatively good agreement between the two, with MRCM colder by 0.92 °C on average. While MRCM temperatures undoubtedly suffer from bias as well, this suggests that the LST correction calculated at the Oukaimeden station and applied to the whole area reasonably succeeds in capturing the overall magnitude of surface air temperature during the wet season. For the most part, the two datasets are within 3 °C of each other, but the difference is largely elevation-dependent. MRCM is colder in the valleys by 1–2 °C, and warmer at high elevations, especially where snow cover is present, by 3–4 °C (Fig. 5). This is likely due to the lack of snow cover in MRCM (largely absent at 12 km resolution) which leads to a warm bias due to snow-albedo feedback, and

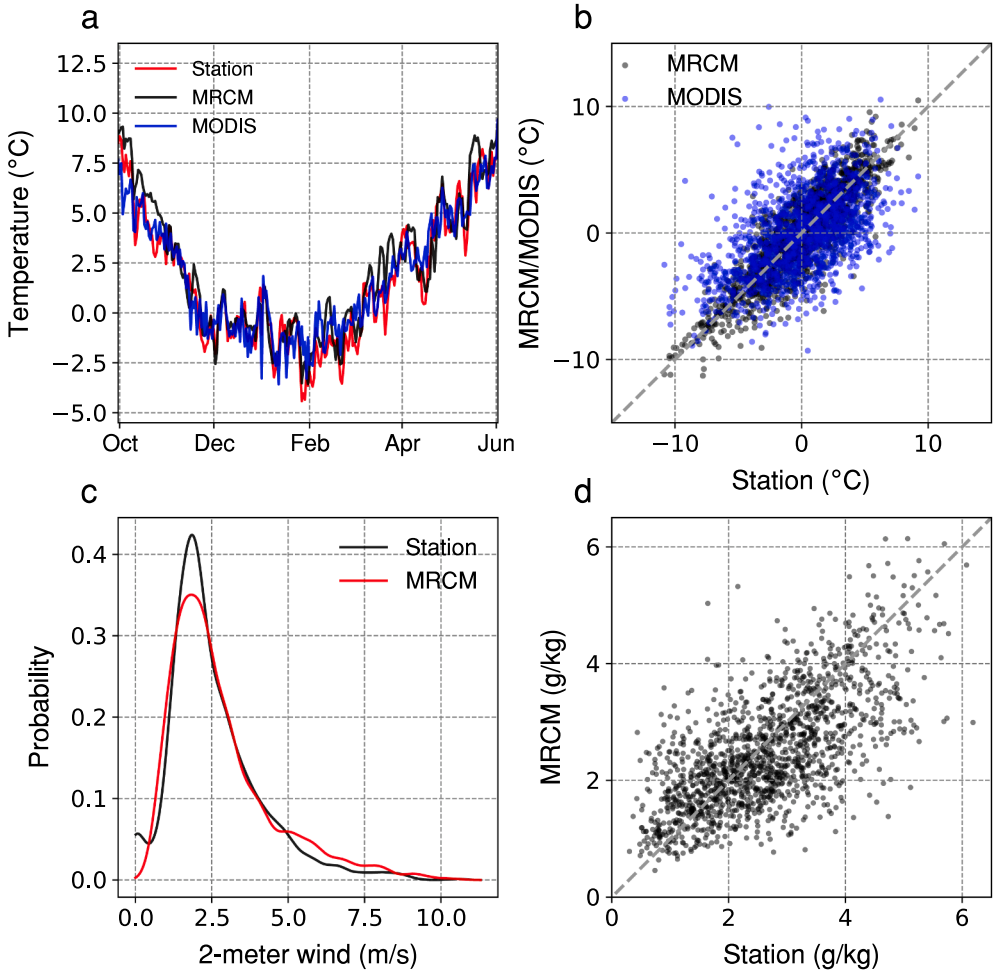

Fig. 6. (a) Average daily temperature during the snowy season (October 1st – June 1st) at the Oukaimeden station: observations (red), MRCM (black) and MODIS LST-derived (blue). (b) Daily air temperature deviations to averages shown in (a): MRCM (black) and MODIS (blue) against observations. (c) Density of October-May daily wind speed at the Oukaimeden station in observations (black) and the MRCM simulation (red). (d) October-May daily specific humidity at the Oukaimeden station: observations against MRCM simulation.

potentially to an uncorrected cold bias in the MODIS data due to the presence of snow at high elevation (Shamir and Georgakakos, 2014). Above-zero air temperatures are frequent at high elevations during winter ($T_a \geq 0$°C 47% of the time between December and March at the Oukaimeden station); in such cases, if snow is on the ground, LST will be colder than the air temperature since the snow surface temperature will not exceed 0 °C. MRCM also fails to capture much of the contrast between north- and south-facing slopes: these are small scale (less than10 km) effects unresolved at the chosen resolution. Our imposed ± 3 °C range around the LST-derived air temperature in the sensitivity data should therefore be enough to capture the "true" air temperature values.

At the Oukaimeden station, the annual cycles of both MRCM and MODIS LST-derived air temperature are in good agreement, with a slight warm bias for MRCM (+0.5 °C) and insignificant bias for MODIS (+0.12 °C), unsurprising here since observations are used to define the linear correction (Fig. 6-a). The spread of daily deviations to each series' annual cycle is also well-captured, although here MRCM performs better (RMSE of 1.8 °C against 3 °C for MODIS) (Fig. 6-b).

MRCM also performs well for daily surface wind and humidity. The correlation of daily 2-meter wind speed with station data is quite low (r = 0.18), but is higher at the monthly time scale (r = 0.59). The distribution of daily wind values also closely follows that of the observations (Fig. 6-c). In addition, daily variability of specific humidity is reasonably captured (correlation of 0.66, bias of 0.1 g/kg and RMSE of 0.8 g/kg, or 33% of the mean), which highlights the performance of MRCM and the accuracy of the downscaling from equation (14).

3.2. Testing the snow model at the Oukaimeden station

The snow model, forced with MODIS LST-derived air temperature, TRMM precipitation, empirical estimates of incoming radiation and MRCM surface wind and humidity, is fitted to the observed snow depth value at the Oukaimeden station. With $M_f = 0.05$, $NMF_{max} = 2.5$ and $TIPM = 0.15$, there is a very good fit between the annual cycles of observed and modeled snow depth (Fig. 7-a). The rapid melt starting in early March is nevertheless faster in the simulation compared to observations. While inter-annual variability is not correctly captured, likely due to TRMM biases, weekly fractional snow cover is not far off from the MODIS estimates (Fig. 7-b). Unsurprisingly, given the characteristic patchiness of snow cover within a grid cell (Baba et al., 2019), MODIS snow cover is often smaller than the fractional coverage inferred from the modeled SWE series (which is itself not perfect). Peak SWE occurs around March 1st, and averages 240 mm in the simulation, against an observed value of 300 mm (Bouamri et al., 2018), a negative bias consistent with that of TRMM precipitation at high elevations. Sublimation losses average 90 mm of water equivalent, or 21.4 ± 4.6% of snowfall, in good agreement with the 25% estimate of López-Moreno et al. (2017) obtained for the same station.

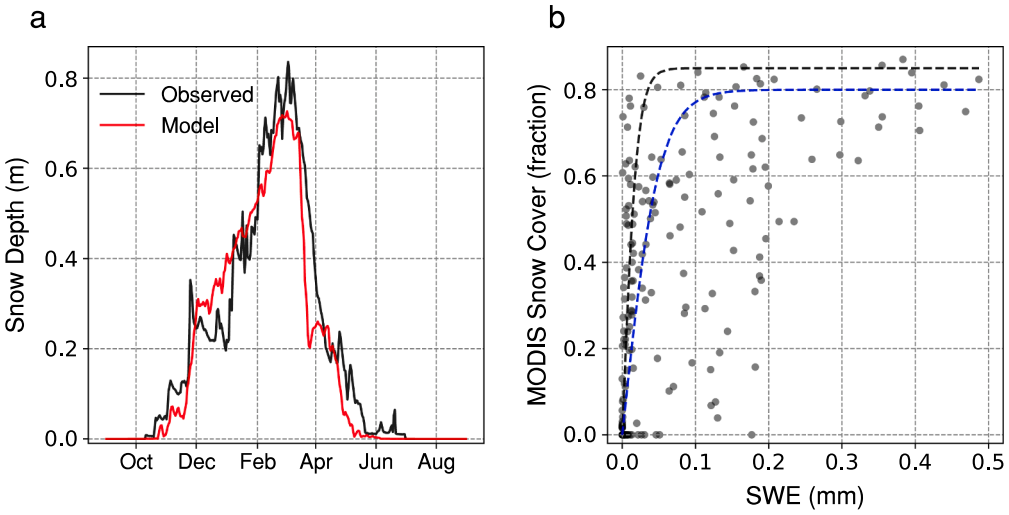

Fig. 7. Results of snow model at Oukaimeden station. (a) Average annual cycle of snow depth (black: observed; red: calibrated model output). (b) Weekly modeled SWE against MODIS fractional snow cover for the corresponding grid cell. The dashed black (respectively blue) line shows the SWE-snow cover relationship defined by equation (10) (respectively (11)).

Table 1
Model parameters: Allowable range and calibrated values for the RTI-SNOW17 model parameters. See Anderson (2006) for details on the selected allowable range.

Parameter	Name	Unit	Range	Value				
				Station	LST + 0	LST-3	LST + 3	TRMM + 33%
M_f	Melt factor	mm/°C/hr	0.001–0.6	0.05	0.06	0.205	0.035	0.08
NMF_{max}	Maximum negative melt factor	mm/°C/hr	0.001–3	2.5	1.2	0.15	2.5	0.3
TIPM	Antecedent temperature index parameter	fraction	0.001–1.0	0.15	0.3	0.91	0.2	0.8

3.3. Comparison of the distributed snow model results to snow cover data

The allowable range and calibrated values of the three model parameters for all basin-wide experiments are given in Table 1. Like Follum et al. (2015), we find that M_f is the most sensitive for the calibration, but that NMF_{max} is slightly more sensitive than *TIPM*. Near the optimal M_f, two or three combinations of NMF_{max} and *TIPM* often yield Nash-Sutcliffe coefficient values not far from the maximum. Thus, while the calibration of M_f is probably more reliable (it is constrained by the observed disappearance of the snowpack once the heat deficit has reached 0), that of the other two parameters should be seen with some caution. In addition, while fitted parameter values for the station experiment may seem similar to those for the LST-3 experiment, they are obtained by optimizing with respect to pointwise observed snow depth, and not MODIS snow cover as in other experiments, and precipitation at the exact station location is not available either. Snow depth at the station may also not be representative of conditions prevailing for the 1 km grid cell.

At the basin scale, the fitted model reproduces much of the characteristics of the snow cover distribution as inferred from the MODIS data. The magnitude and variability of snow cover are well approximated, both at the daily and seasonal timescale (Fig. 8). Some short-term peaks in snow cover are underestimated, as in January 2007 (Fig. 8-b), or overestimated, as in March 2009 (Fig. 8-c). This is not unexpected given the uncertainty in the forcing data. One should also remember that MODIS snow cover is itself an imperfect measure of snowpack extent, even when averaged at the weekly timescale. Non-missing data is not free of errors and the filtering algorithm implemented here may fail in certain circumstances (e.g., particularly persistent cloud cover) (Baba et al., 2019).

Looking at different elevation ranges, we find that mean snow cover and its inter-annual variability are also well reproduced (Fig. 8-d and

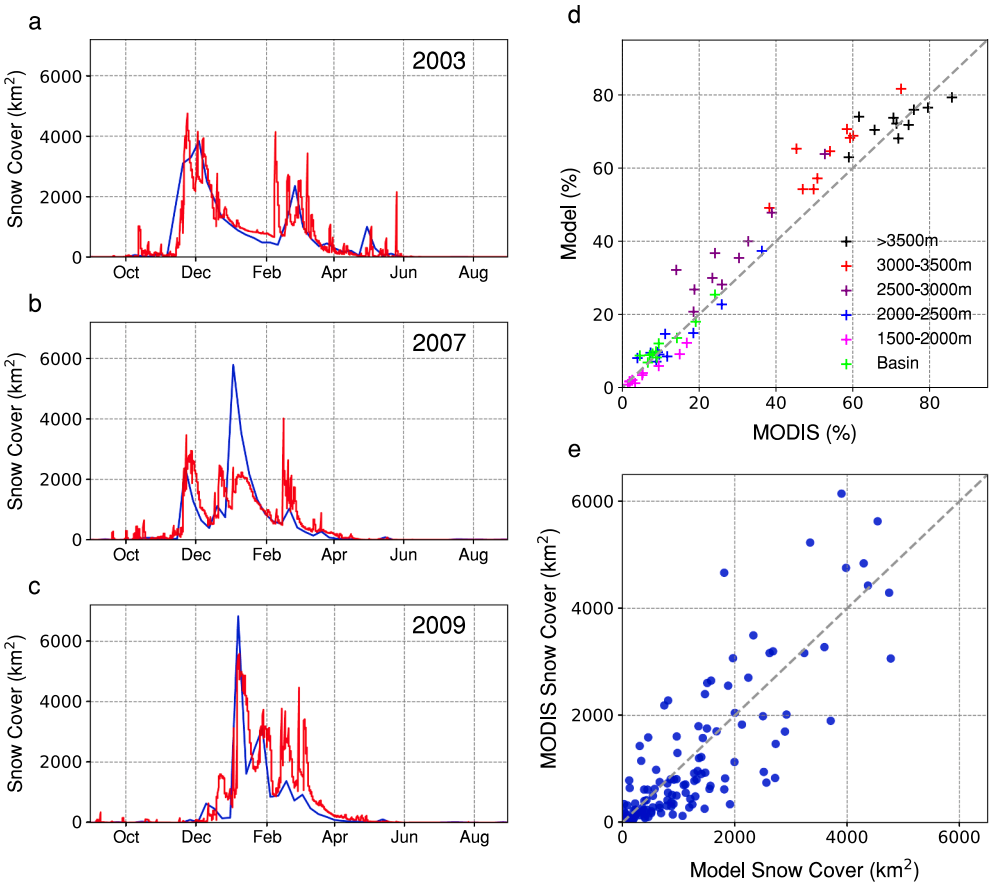

Fig. 8. Snow model results for the control experiment. (a-c) Daily snow cover extent from model simulations (red) and weekly extent from the MOD10A1 dataset (blue) for three hydrological years (shown top-right): (a) 2003–04, (b) 2007–08 and (c) 2009–10. (d) December-March average snow cover (in %) in model simulations and MOD10A1 data, for all 10 hydrological years of the simulations, at various elevation ranges. (e) Weekly modeled snow cover extent against MOD10A1 estimates (2001–2011).

9), particularly the timing and speed of snowpack build-up and melt. Still, the model tends to overestimate snow cover at high elevations (≥2500 m) and underestimate it at low elevations. The latter is not particularly critical since snow cover below 1500 m is mostly scarce and short-lived, and stores little to no water over the winter season. The former, however, suggests an overestimation of the snow water content, or an inadequacy of our SWE-fractional snow cover relationship. For a given SWE, we may be underestimating the variability of snow cover below 1 km, and therefore falsely inflating the corresponding fractional snow cover.

The fraction of snow to total precipitation is also useful to consider. Based on the MODIS LST-derived air temperature, the fraction of snowfall to annual precipitation ranges from 2 to 3% at the lowest elevations (~800 m) to more than 65% near the highest peaks (Fig. 10-b). Areas above 2500 m, which account for most of the snowpack, receive about 52% (respectively 75%) of their annual (respectively November-April) precipitation as snow. The comparison with the CAF station figures (snowfall is 50% of annual and 68% of November-April precipitation, Fig, 10-d) suggests that the MODIS LST-derived air temperature may still be positively biased with respect to real-world T_a. The higher snow fractions in the LST-3 run are indeed closer to observed values. Another possibility is that precipitation is preferentially underestimated when it is solid, a common problem with satellite-based estimates (Derin et al., 2016; Fayad et al., 2017), thus automatically decreasing the fraction of snow to annual precipitation.

3.4. Snow model output: Latent heat fluxes

The High Atlas is characterized by rather dry conditions, even at high altitudes during winter: for instance, the average relative humidity between December and March at the Oukaimeden station (3200 m asl) is only 46%. Together with persistent snow cover above 2500 m and occasional strong winds (Fig. 6-c), conditions are met for large latent heat fluxes. In the control (LST + 0) simulation, we find for the basin as a whole that snowpack losses by sublimation amount to 0.095 km^3 on average, which is small compared to total precipitation (1.9% of annual precipitation, 2.8% of November-April precipitation) and to the total snowfall (~9%). Relative losses increase rapidly with elevation, from only 5% at 2000 m to about 30% above 3500 m (Fig. 10-d). Near 3200 m altitude, sublimation removes 20% of the snowpack, not far from the 25% found by López-Moreno et al. (2017) at Oukaimeden. Still, the difference remains significant. Part of it may be due to the fact that the latitude of our domain is slightly higher and relative humidity is consequently larger (46% at Oukaimeden vs. 54% at similar locations in our domain). At 12 km, the resolution of our downscaled regional climate simulations remains coarse for snowpack modeling and therefore wind speed at high elevations may also be underestimated, a possibility that would require additional wind measurements to verify. Inter-annual variability in sublimation losses is substantial: they vary between 18% and 42% above 3500 m, and, even below 2000 m, range from 1 to 5%.

These estimates are naturally very dependent on the wind, humidity and temperature data used as forcing. They are about a third lower in the LST-3 simulation compared to LST + 0, and half again as much in LST + 3, but display the same strong dependence to elevation (Fig. 10-d). For instance, above 3000 m, 21% of the snowpack is lost to sublimation on average in LST + 0, 14% in LST-3 and 32% in LST + 3.

3.5. Snow model output: basin-wide SWE volume

Although no basin-wide SWE observations are available, it is useful to estimate the total snowpack water content inferred by the model constrained by the observed snow cover. The average annual cycle of basin-wide SWE is shown on Fig. 11-a. The build-up of the snowpack is

gradual, starting in early November; a peak is reached around February 1st followed by melting ending in mid-May. At its peak, basin-wide SWE reaches 150 million cubic meters (MCM), or 0.15 km^3 (Fig. 11-a). This is a small fraction of cumulative snowfall for the area, which amounts to roughly 1 km^3. Due to the high inter-annual variability of precipitation, the SWE peak can range anywhere from 50 to 450 MCM, a much larger variability than that of precipitation. Most of the snowpack, even at its peak, is concentrated above 2500 m, an area which covers about 15% of the whole basin (Fig. 11-b). Despite frequent snowfall, areas below 2000 m are insignificant in terms of water equivalent. Melt is rapid, essentially occurring between February and May (Fig. 11-d), when temperatures quickly rise above freezing at all altitudes. However, even during winter, positive temperatures are frequent and this is reflected in non-negligible melt rates throughout the snowy season. Our model indicates an average cumulative melt of 260 MCM between October and June.

3.6. Sensitivity to input data and modeling assumptions

Finally, we turn to the sensitivity analysis of basin-wide SWE and snow water balance to uncertainties in the forcing data and to the SWE-snow cover relationship. Optimal parameters are found for each experiment so that they all reproduce basin-wide and elevation-specific snow cover series, though most (except LST + 3 and the SC40 experiments) tend to overestimate snow cover between 2500 and 3000 m (as in Fig. 9). The build-up of the snowpack is also too slow in the SC40 run, no doubt due to the larger SWE required to reach maximum snow cover (section 2.4). However, constrained as they are by the observed snow cover series, the various experiments all show somewhat similar basin-wide SWE values, between 120 and 210 MCM at their peaks (Fig. 11-c). The maximum peak SWE is unsurprisingly attained in the SC40 experiment, since it requires a higher SWE to attain the same fractional snow cover. This still amount to a significant uncertainty, which is difficult to resolve. An empirical backward SWE reconstruction constrained by the evolution of the snow cover (Fayad et al., 2017) may be useful as a future step to test the validity of our SWE results, for instance using higher-resolution Sentinel data. Additional station data, even at low elevations, would be helpful to improve temperature estimates. Because our approach uses snow cover to fit the snow model, the SWE-snow cover relationship is a major source of variability in the results, as we see in the case of the SC40 experiment. In the control formulation, maximum cell snow cover is reached for 5 mm SWE, roughly 15–40 cm of snow depth. Increasing that threshold to 10 mm as in SC40 increases peak basin-wide SWE by 60MCM, and therefore the extreme case of a 20 mm threshold could potentially bring the result up to 300MCM, or double what we found in the control experiment. The analysis of spring runoff volumes could help put an upper bound on that figure.Fig. 10

Precipitation biases, however, are more challenging to tackle with no high-altitude data at hand. Statistical models to correct and distribute precipitation within a TRMM grid cell based on fine-scale topography may help resolve some of the biases due to the complexity of the terrain at small scales. Another possibility would be to calibrate additional parameters in SNOW17 which we took constant here, in particular the temperature threshold to define snowfall and a precipitation under-catch adjustment factor (Follum et al., 2015). Still, the potential underestimation of precipitation does not seem to impact the SWE estimates very much: they are only about 10% higher in the TRMM + 33% experiment than in the control run. In the absence of station data, it is difficult to determine whether this correction is

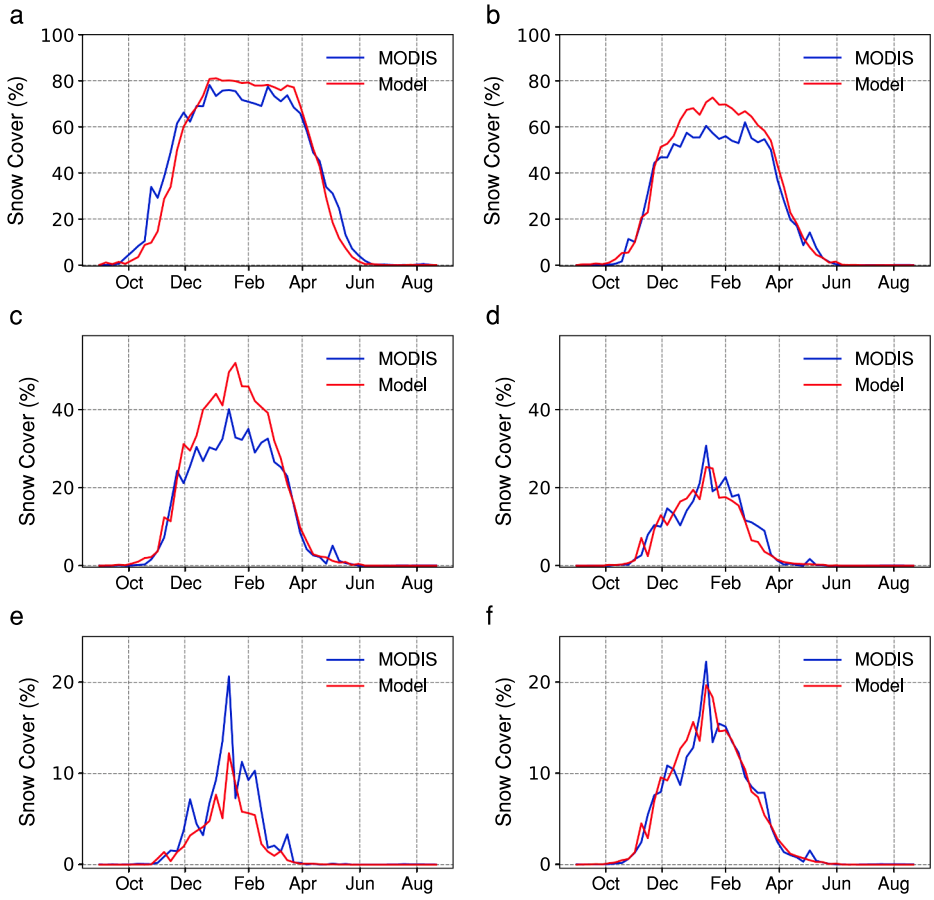

Fig. 9. Average annual cycle of snow cover (in %) in the control experiment at various elevations ranges within our study area: (a) > 3500 m, (b) 3000–3500 m, (c) 2500–3000 m, (d) 2000–2500 m, (e) 1500–2000 m and (f) whole area.

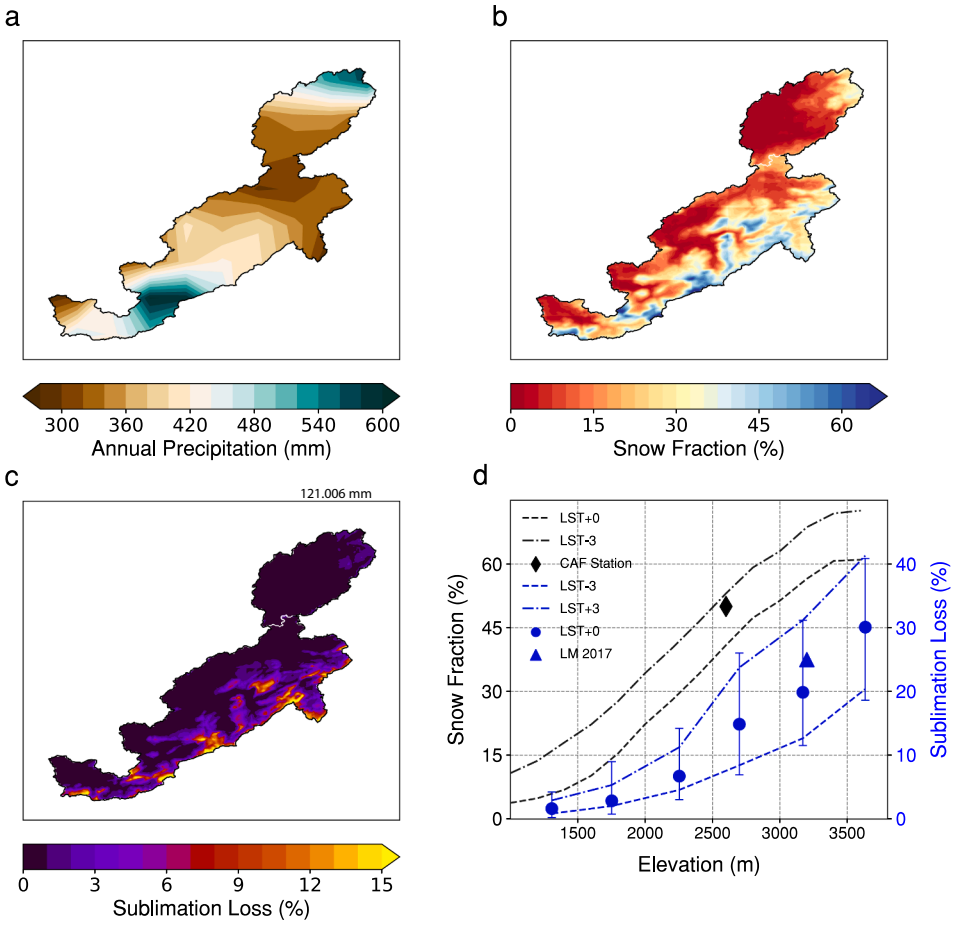

Fig. 10. (a) Annual precipitation (TRMM). (b) Fraction of annual precipitation falling as snow. (c) Fraction of annual precipitation lost by sublimation. (d) Fraction of annual precipitation falling as snow (black, left axis) and fraction of snowfall lost to sublimation (blue, right axis) as a function of elevation. Estimated values for the CAF station and Oukaimeden experimental site are also shown. Data for (a-b) is from the control (LST + 0) experiment. LM 2017 = Lopez-Moreno et al. (2017).

enough to compensate for underestimated or even missing snowfall episodes in the TRMM data; results by Hashemi et al. (2017) over the United States suggest that winter precipitation above 3000 m altitude may be underestimated by as much as 50%. For a fixed SWE-snow cover relationship, the impact of precipitation uncertainty on peak SWE seems small (Fig. 11-c), though it would matter for melting rates: too much precipitation at fixed snow cover may lead to overestimation of melt during the cold season.

As discussed previously, sublimation rates are also uncertain, mainly because of biases in air temperature and surface wind speed. The low rates found in the LST-3 experiment seem unlikely based on what is known in such environments (López-Moreno et al., 2017), and our 20% estimate above 3000 m is probably at the low end of the range. Rates of 45% were measured on the southward, much drier side of the Atlas, thus setting an upper bound to what can reasonably be expected in our region. Overall, a 20–35% range is realistic.

4. Conclusion

This study offers the first implementation of a distributed, physically-based empirical snow model at large scale in the High Atlas of Morocco. This region is characterized by a very sparse station network, and therefore we relied on satellite-based and dynamically-downscaled meteorological data as forcing for the SNOW-17 model, and compared the model simulated snow cover to remotely-sensed snow cover estimates from MODIS. The model accurately captures the distribution of snow cover at various elevation bands as well as its temporal dynamics. When applied at the Oukaimeden station, results were also consistent. While our coarse resolution and the numerous uncertainties associated with the forcing data bring important limitations to our results, we find reasonable confidence in a basin-wide average SWE of 0.15–0.175 km^3, almost exclusively concentrated above the 2500 m altitude line. We also find that sublimation losses are substantial, ranging from 0.06 to 0.14 km^3 for the whole basin and amounting on average to 20% of total snowfall above 3000 m, in keeping with previous results (López-Moreno et al., 2017). Our results offer a first-order estimate of sublimation in the High Atlas, in absence of even a sparse network of direct sublimation observations. In addition, the model offers the potential for assessing the sensitivity of High Atlas snowpack to climate change, of critical importance for the region. Many improvements to our approach are possible, whether regarding the selection and correction of data or the modeling itself, and the advent of higher-resolution snow cover estimates with Sentinel-5 will certainly help in this direction (Baba et al., 2019). However, as long as station observations remain so scarce, any estimate of snow dynamics in the High Atlas will remain quite uncertain. In particular, more direct measurements of latent heat fluxes are necessary to validate sublimation parametrizations and modeled fluxes in this region.

CRediT authorship contribution statement

Alexandre Tuel: Conceptualization, Methodology, Software, Visualization, Writing - original draft. **Abdelghani Chehbouni:** Resources, Writing - review & editing. **Elfatih A.B. Eltahir:** Conceptualization, Methodology, Supervision, Writing - review & editing.

Declaration of Competing Interest

The authors declare that they have no known competing financial interests or personal relationships that could have appeared to influence the work reported in this paper.

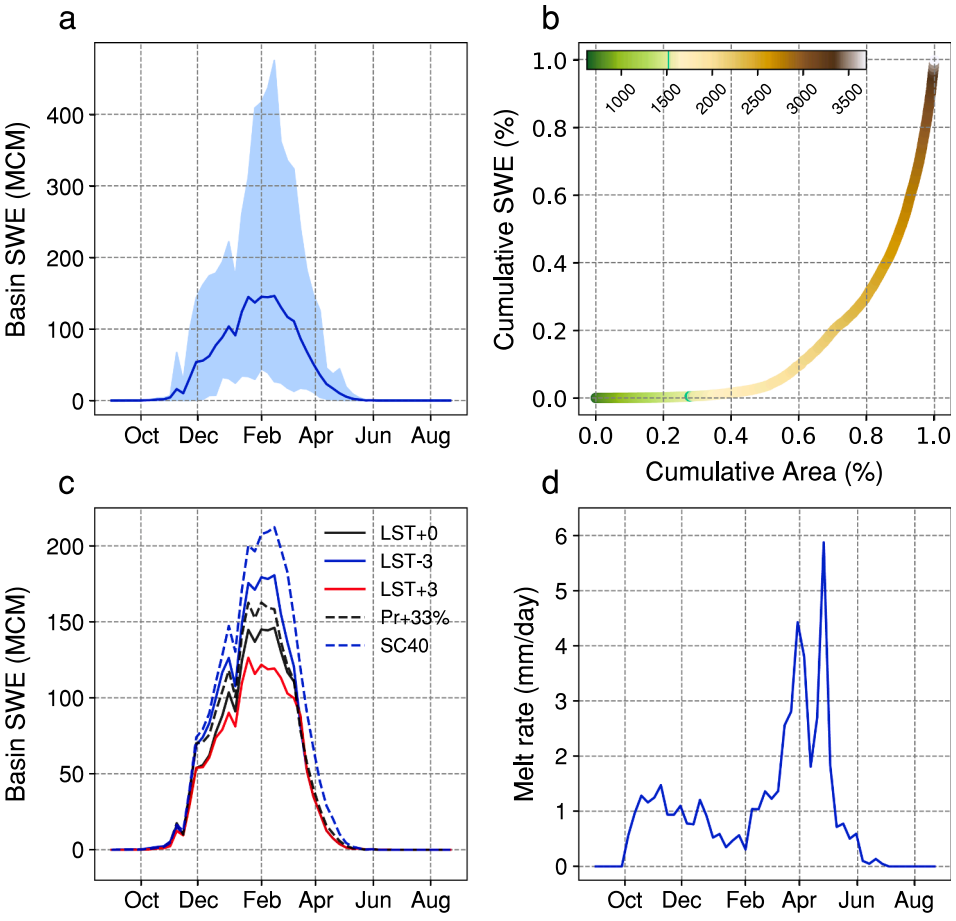

Fig. 11. (a) Annual cycle of basin-wide SWE in the control experiment: mean (solid blue) and 90% range (blue shading). (b) Cumulative distribution function of basin area (x-axis) and peak SWE (y-axis) as a function of elevation (shading). Basin area and peak SWE were both renormalized by their maxima to make the two axes equal. (c) Annual cycles of basin-wide SWE in the various sensitivity experiments. (d) Annual cycle of average daily melt rate for areas with positive snow cover.

Acknowledgements

This work was made possible through funding from the Office Chérifien des Phosphates (OCP) through Université Mohamed VI Polytechnique, Morocco. The authors would like to thank Michael Follum and Jeffrey Niemann for providing their RTI-SNOW17 code and Abdelghani Boudhar and Chakir Adnane from LMI TREMA for sharing the Oukaimeden station data.

References

Ackerman, S., Strabala, K., Menzel, P., Frey, R., Moeller, C., Gumley, L., 1998. Discriminating clear sky from clouds with MODIS. J. Geophys. Res. 103, 141–157. https://doi.org/10.1029/1998JD200032.

Alduchov, O.A., Eskridge, R.E., 1996. Improved Magnus Form Approximation of Saturation Vapor Pressure. J. Appl. Meteor. 35, 601–609. https://doi.org/10.1175/1520-0450(1996)035<0601:IMFAOS>2.0.CO;2.

Alonso-González, E., López-Moreno, J.I., Gascoin, S., García-Valdecasas Ojeda, M., Sanmiguel-Vallelado, A., Navarro-Serrano, F., Revuelto, J., Ceballos, A., Esteban-Parra, M.J., Essery, R., 2018. Daily gridded datasets of snow depth and snow water equivalent for the Iberian Peninsula from 1980 to 2014. Earth Syst. Sci. Data 10, 303–315. https://doi.org/10.5194/essd-10-303-2018.

Anderson, E.A., 1976. A Point of Energy and Mass Balance Model of Snow Cover. U.S. National Oceanic and Atmospheric Administration NOAA Technical Report NWS 19, Silver Spring, MD.

Anderson, E.A., 2006. Snow Accumulation and Ablation Model – SNOW-17, NWSRFS User Documentation. U.S. National Weather Service, Silver Springs, MD. http://www.nws.noaa.gov/oh/hrl/nwsrfs/users_manual/part2/_pdf/22snow17.pdf.

Baba, M.W., Gascoin, S., Kinnard, C., Marchane, A., Hanich, L., 2019 Effect of digital elevation model resolution on the simulation of the snow cover evolution in the High Atlas. Water Resources Research, 55. http://dx.doi.org/10.1029/2018WR023789.

Bouamri, H., Boudhar, A., Gascoin, S., Kinnard, C., 2018. Performance of temperature and radiation index models for point-scale snow water equivalent (SWE) simulations in the Moroccan High Atlas Mountains. Hydrol. Sci. J. 63 (12), 1844–1862. https://doi.org/10.1080/02626667.2018.1520391.

Boudhar, A., et al., 2009. Evaluation of the snowmelt runoff model in the Moroccan high Atlas Mountains using two snow-cover estimates. Hydrol. Sci. J. 54, 1094–1113. https://doi.org/10.1623/hysj.54.6.1094.

Boudhar, A., Duchemin, B., Hanich, L., Jarlan, L., Chaponnière, A., Maisongrande, P., Boulet, G., Chehbouni, A., 2010. Long term analysis of snow-covered-area in the Moroccan High-Atlas through remote sensing. Int. J. Appl. Earth Obs. Geoinf. S109–S115. https://doi.org/10.1016/j.jag.2009.09.008.

Boudhar, A., Duchemin, B., Hanich, L., Boulet, G., Chehbouni, A., 2011. Spatial distribution of the air temperature in mountainous areas using satellite thermal infra-red data. C. R. Geoscience 343, 32–42.

Boudhar, A., Boulet, G., Hanich, L., Sicart, J.-E., Chehbouni, A., 2016. Energy fluxes and melt rate of a seasonal snow cover in the Moroccan High Atlas. Hydrol. Sci. J. 61 (5), 931–943. https://doi.org/10.1080/02626667.2014.965173.

Brock, B.W., Willis, I.C., Sharp, M.J., 2000. Measurement and parameterization of albedo variations at Haut Glacier d'Arolla, Switzerland. J. Glaciol. 46, 675–688. https://doi.org/10.3189/172756500781832675.

Brutsaert, W., 1982. Evaporation into the atmosphere. Theory, history and application. Dordrecht: Kluwer Academic. http://dx.doi.org/10.1007/978-94-017-1497-6.

Carroll, T.R., Cline, D.W., Olheiser, C., Rost, A., Nilsson, A., Fall, G., Bovitz, C., Li, L., 2006. NOAA's national snow analyses. Proceedings of the 74th Annual Meeting of the Western Snow Conference 74:13.

Chehbouni, A., et al., 2008. An integrated modelling and remote sensing approach for hydrological study in arid and semi-arid regions: the SUDMED program. Int. J. Remote Sens. 29, 5161–5181. https://doi.org/10.1080/01431160802036417.

Clark, M.P., Hendrikx, J., Slater, A.G., Kavetski, D., Anderson, B., Cullen, N.J., Kerr, T., Örn Hreinsson, E., Woods, R.A., 2011. Representing spatial variability of snow water equivalent in hydrologic and land-surface models: A review. Water Resour. Res. 47, W07539. https://doi.org/10.1029/2011WR010745.

Derin, Y., Anagnostou, E., Berne, A., Borga, M., Boudevillain, B., Buytaert, W., Chang, C., Delrieu, G., Hong, Y., Hsu, Y.C., Lavado-Casimiro, W., Manz, B., Moges, S., Nikolopoulos, E.I., Sahlu, D., Salerno, F., Rodríguez-Sánchez, J., Vergara, H.J., Yilmaz, K.K., 2016. Multiregional Satellite Precipitation Products Evaluation over Complex Terrain. J. Hydrometeor. 17, 1817–1836. https://doi.org/10.1175/JHM-D-15-0197.1.

Downer, C.W., Ogden, F.L., Niedzialek, J.M., Liu, S., 2006. Gridded Surface/Subsurface Hydrologic Analysis (GSSHA) model: a model for simulating diverse streamflow producing processes. In: Singh, V.P., Frevert, D.K. (Eds.), Watershed Models. Taylor & Francis, CRC Press, Boca Raton, FL, pp. 131–157.

Duffie, J.A., Beckman, W.A., 2013. Solar Engineering of Thermal Processes, Fourth Edition. Wiley, New York. https://dx.doi.org/10.1002/9781118671603.

Fassnacht, S., et al., 2017. Spatio-temporal snowmelt variability across the headwaters of the Southern Rocky Mountains. Frontiers of Earth Science 11 (3), 505–514. https://doi.org/10.1007/s11707-017-0641-4.

Fayad, A., et al., 2017. Snow hydrology in Mediterranean mountain regions: a review. J. Hydrol. 551, 374–396. https://doi.org/10.1016/j.jhydrol.2017.05.063.
Follum, M.L., Downer, C.W., Niemann, J.D., Roylance, S.M., Vuyovich, C.M., 2015. A radiation-derived temperature-index snow routine for the GSSHA hydrologic model. J. Hydrology 529, 723–736. https://doi.org/10.1016/j.jhydrol.2015.08.044.
Follum, M.L., Niemann, J.D., Fassnacht, S.R., 2019. A comparison of snowmelt-derived streamflow from temperature-index and modified-temperature-index snow models. Hydrol. Process. 33, 3030–3045. https://doi.org/10.1002/hyp.13545.
Franz, K., Butcher, P., Ajami, N., 2010. Addressing snow model uncertainty for hydrologic prediction. Adv. Water Resour. 33, 820–832. https://doi.org/10.1016/j.advwatres.2010.05.004.
Funk, C., Peterson, P., Landsfeld, M., et al., 2015. The climate hazards infrared precipitation with stations—a new environmental record for monitoring extremes. Sci Data 2, 150066. https://doi.org/10.1038/sdata.2015.66.
Guan, B., Molotch, N., Waliser, D., Jepsen, S., Painter, T., Dozier, J., 2013. Snow water equivalent in the Sierra Nevada: Blending snow sensor observations with snowmelt model simulations. Water Resour. Res. 49, 5029–5046. https://doi.org/10.1002/wrcr.20387.
Hachem, S., Duguay, C.R., Allard, M., 2012. Comparison of MODIS-derived land surface temperature with ground surface and air temperature measurements in continuous permafrost terrain. The Cryosphere 6, 51–69. https://doi.org/10.5194/tc-6-1-2012.
Hall, D.K., Box, J.E., Casey, K.A., Hook, S.J., Schuman, C.A., Steffen, K., 2008. Comparison of satellite derived and in-situ observations of ice and snow surface temperatures over Greenland. Remote Sens. Environ. 112, 3739–3749. https://doi.org/10.1016/j.rse.2008.05.007.
Hall, D. K., Riggs, G. A., 2016. MODIS/Terra Snow Cover Daily L3 Global 500m SIN Grid, Version 6. [MOD10A1]. Boulder, Colorado USA. NASA National Snow and Ice Data Center Distributed Active Archive Center. http://dx.doi.org/10.5067/MODIS/MOD10A1.006.
Hashemi, H., Nordin, M., Lakshmi, V., Huffman, G.J., Knight, R., 2017. Bias Correction of Long-Term Satellite Monthly Precipitation Product (TRMM 3B43) over the Conterminous United States. J. Hydrometeor. 18, 2491–2509. https://doi.org/10.1175/JHM-D-17-0025.1.
He, M., Hogue, T.S., Franz, K.J., Margulis, S.A., Vrugt, J.A., 2011. Characterizing parameter sensitivity and uncertainty for a snow model across hydroclimatic regimes. Adv. Water Resour. 34 (1), 114–127. https://doi.org/10.1016/j.advwatres.2010.10.002.
Hedstrom, N., Pomeroy, J.W., 1998. Measurements and modelling of snow interception in the boreal forest. Hydrol. Process. 12, 1611–1625 https://doi.org/10.1002/(SICI)1099-1085(199808/09)12:10/11 < 1611::AID-HYP684 > 3.0.CO;2-4.
Herrero, J., Polo, M.J., 2016. Evaposublimation from the snow in the Mediterranean mountains of Sierra Nevada (Spain). The Cryosphere 10 (6), 2981–2998. https://doi.org/10.5194/tc-10-2981-2016.
Hock, R., 1999. A distributed temperature-index ice- and snowmelt model including potential direct solar radiation. J. Glaciol. 45, 101–111. https://doi.org/10.1017/S0022143000003087.
Huffman, G. J., Bolvin, D., Braithwaite, D., Hsu, F., Joyce, R., Xie, P., 2014. Integrated Multi- satellitE Retrievals for GPM (IMERG), version 4.4.
Huffman, G.J., Bolvin, D.T., Nelkin, E.J., Wolff, D.B., Adler, R.F., Gu, G., Hong, Y., Bowman, K.P., Stocker, E.F., 2007. The TRMM Multisatellite Precipitation Analysis (TMPA): Quasi-Global, Multiyear, Combined-Sensor Precipitation Estimates at Fine Scales. J. Hydrometeor. 8, 38–55. https://doi.org/10.1175/JHM560.1.
Huffman, G.J., Adler, R.F., Morrissey, M.M., Curtis, S., Joyce, R., McGavock, B., Susskind, J., 2001. Global precipitation at one-degree daily resolution from multi-satellite observations. J. Hydrometeor. 2, 36–50 10.1175/1525-7541(2001)002 < 0036:GPAODD > 2.0.CO;2.
Jarvis, A., Reuter, H. I., Nelson, A., Guevara, E., 2008. Hole-filled SRTM for the globe Version 4, available from the CGIAR-CSI SRTM 90m Database (available at http://srtm.csi.cgiar.org/srtmdata/).
Knippertz, P., Christoph, M., Speth, P., 2003. Long-term precipitation variability in Morocco and the link to the large-scale circulation in recent and future climates. Meteorol. Atmos. Phys. 83, 67–88. https://doi.org/10.1007/s00703-002-0561-y.
Liston, G.E., Elder, K., 2006. A distributed snow-evolution modeling system (SnowModel). J. Hydrometeorol. 7 (6), 1259–1276. https://doi.org/10.1175/JHM548.1.
López-Moreno, J.I., Gascoin, S., Herrero, J., Sproles, E.A., Pons, M., Alonso-González, E., Hanich, L., Boudhar, A., Musselman, K.N., Molotch, N.P., Sickman, J., Pomeroy, J., 2017. Different sensitivities of snowpacks to warming in Mediterranean climate mountain areas. Environ. Res. Lett. 12, 074006. https://doi.org/10.1088/1748-9326/aa70cb.
Marchane, A., Jarlan, L., Hanich, L., Boudhar, A., Gascoin, S., Tavernier, A., Filali, N., Le Page, M., Hagolle, O., Berjamy, B., 2015. Assessment of daily MODIS snow cover products to monitor snow cover dynamics over the Moroccan Atlas mountain range. Remote Sens. Environ. 160, 72–86. https://doi.org/10.1016/j.rse.2015.01.002.
Marchane, A., Jarlan, L., Boudhar, A., Tramblay, Y., Hanich, L., 2016. Linkages between snow cover, temperature and rainfall and the North Atlantic Oscillation over Morocco. Clim. Res. 69, 229–238. https://doi.org/10.3354/cr01409.
Marks, D., Domingo, J., Susong, D., Link, T., Garen, D., 1999. A spatially distributed energy balance snowmelt model for application in mountain basins. Hydrol. Process. 13, 1935–1959.
Milewski, A., Elkadiri, R., Durham, M., 2015. Assessment and comparison of TMPA satellite precipitation products in varying climatic and topographic regimes in Morocco. Remote Sens. 7, 5697–5717. https://doi.org/10.3390/rs70505697.
Molotch, N.P., 2009. Reconstructing snow water equivalent in the Rio Grande headwaters using remotely sensed snow cover data and a spatially distributed snowmelt model. Hydrol. Process. 23, 1076–1089. https://doi.org/10.1002/hyp.7206.
Molotch, N.P., Margulis, S.A., 2008. Estimating the distribution of snow water equivalent using remotely sensed snow cover data and a spatially distributed snowmelt model: A multi-resolution, multi-sensor comparison. Adv. Wat. Res. 31, 1503–1514. https://doi.org/10.1016/j.advwatres.2008.07.017.
Muñoz, E., Arumí, J. L., Rivera, D., Montecinos, A., Billib, M., Álvarez, C. Gridded data for a hydrological model in a scarce-data basin. Water Management 167(5), 249-258. http://dx.doi.org/10.1680/wama.12.00086.
Nash, J.E., Sutcliffe, J.V., 1970. River flow forecasting through conceptual models. Part I — A discussion of principles. J. Hydrol. 10 (3), 282–290. https://doi.org/10.1016/0022-1694(70)90255-6.
Ouatiki, H., Boudhar, A., Tramblay, Y., Jarlan, L., Benabdelouhab, T., Hanich, L., El Meslouhi, M.R., Chehbouni, A., 2017. Evaluation of TRMM 3B42 V7 Rainfall Product over the Oum Er Rbia Watershed in Morocco. Climate 5 (1). https://doi.org/10.3390/cli5010001.
Platnick, S., Ackerman, S.A., King, M.D., Meyer, K., Menzel, W.P., Holz, R.E., Baum, B.A., Yang, P., 2015. MODIS atmosphere L2 cloud product (06_L2). NASA MODIS Adaptive Processing System, Goddard Space Flight Center. https://doi.org/10.5067/MODIS/MOD06_L2.006.
Raleigh, M.S., Lundquist, J.D., 2012. Comparing and combining SWE estimates from the SNOW-17 model using PRISM and SWE reconstruction. Water Resour. Res. 48, W01506. https://doi.org/10.1029/2011WR010542.
Schulz, O., de Jong, C., 2004. Snowmelt and sublimation: field experiments and modelling in the High Atlas Mountains of Morocco. Hydrol. Earth Syst. Sci. 8, 1076–1089. https://doi.org/10.5194/hess-8-1076-2004.
Shamir, E., Georgakakos, K.P., 2007. Estimating snow depletion curves for American River basins using distributed snow modeling. J. Hydrol. 334 (1), 162–173. https://doi.org/10.1016/j.jhydrol.2006.10.007.
Shamir, E., Georgakakos, K.P., 2014. MODIS Land Surface Temperature as an index of surface air temperature for operational snowpack estimation. Remote Sens. Environ. 152, 83–98. https://doi.org/10.1016/10.1016/j.rse.2014.06.001.
Strasser, U., Bernhardt, M., Weber, M., Liston, G.E., Mauser, W., 2008. Is snow sublimation important in the alpine water balance? Cryosphere 2, 53–66. https://doi.org/10.5194/tc-2-53-2008.
Tuel, A., Eltahir, E.A., 2018. Seasonal precipitation forecast over Morocco. Water Resour. Res. 54. https://doi.org/10.1029/2018WR022984.
Tuel, A., Eltahir, E.A., 2020. Why is the Mediterranean a Climate Change Hot Spot? J. Clim. 33 (14), 5829–5843. https://doi.org/10.1175/JCLI-D-19-0910.1.
Tuel, A., Kang, S., Eltahir, E. A. B., 2020. Understanding Climate Change over the Western Mediterranean Using High-Resolution Simulations, submitted to Climate Dynamics.
Wan, Z., 2008. New refinements and validation of the MODIS land surface temperature/emissivity products. Remote Sens. Environ. 112, 59–74. https://doi.org/10.1016/j.rse.2006.06.026.
Wan, Z., Hook, S., Hulley, G., 2015. MOD11A1 MODIS/Terra Land Surface Temperature/Emissivity Daily L3 Global 1km SIN Grid V006, distributed by NASA EOSDIS Land Processes DAAC, https://dx.doi.org/10.5067/MODIS/MOD11A1.006.
Wang, Y., Wang, M., Zhao, J., 2013. A comparison of MODIS LST retrievals with in situ observations from AWS over the Lambert Glacier Basin, East Antarctica. Int. J. Geosci. 4, 611–617. https://doi.org/10.4236/ijg.2013.43056.
Williamson, S.N., Hik, D.S., Gamon, J.A., Kavanaugh, J.L., Flowers, G.E., 2014. Estimating Temperature Fields from MODIS Land Surface Temperature and Air Temperature Observations in a Sub-Arctic Alpine Environment. Remote Sens. 6, 946–963. https://doi.org/10.3390/rs6020946.
Wrzesien, M.L., Durand, M.T., Pavelsky, T.M., Howat, I.M., Margulis, S.A., Huning, L.S., 2017. Comparison of Methods to Estimate Snow Water Equivalent at the Mountain Range Scale: A Case Study of the California Sierra Nevada. J. Hydrometeorol. 18, 1101–1119. https://doi.org/10.1175/JHM-D-16-0246.1.
Xu, Y., 2018. Evaluation of mineral dust aerosol optical depth and related components from the CHIMERE-DUST model using satellite remote sensing and ground-based observations. Atmos. Environ. 191, 395–413. https://doi.org/10.1016/j.atmosenv.2018.03.061.